

Simplified Model for Description of HVOF NiCr Coating Properties Through Experimental Design and Diagnostic Measurements

D. Zois, T. Wentz, R. Dey, S. Sampath, and C.M. Weyant

(Submitted June 26, 2012; in revised form January 2, 2013)

The use of factorial design in process parameter development allowed determination of the contribution of key process variables, such as flame energy (combustion pressure and O_2/F), spray distance, and feed rate, on in-flight particle properties. The significance of each parameter was used to construct a simple model which enabled the description of particles' temperature and velocity. Particles with velocities ranging by as much as 300 m/s and temperatures ranging up to 350 °C were used to produce an array of coatings on an in situ curvature sensor enabling the determination of the evolving—during spraying—and residual stress at the end of the process, correspondingly. These diverse particle states combined with the flame impingement on the substrate, resulted in coatings of similar thickness, but significantly different stress states. Real time evolving stresses—during deposition—and coating properties such as, microhardness, modulus, and corrosion behavior were correlated to particle in-flight properties and, via the use of the introduced model, to spray parameters.

Keywords corrosion, design of experiment (DOE), HVOF, influence of spray parameters, in situ monitoring, Ni-Cr, residual stress

1. Introduction

It is widely accepted that residual stresses in thermally sprayed coatings play a significant role in processing, properties, and overall performance. Over the last two decades several investigations have supported this (Ref 1-3) for both APS (Ref 4, 5) and HVOF spraying processes (Ref 6, 7). Moreover, specialized equipment (Ref 2, 4) has been developed recently, capable of not only measuring the residual stress but distinguishing between the spraying (or deposition stress) and thermal (or cooling stress)

This article is an invited paper selected from presentations at the 2012 International Thermal Spray Conference and has been expanded from the original presentation. It is simultaneously published in *Thermal Spray 2012: Proceedings of the International Thermal Spray Conference, Air, Land, Water, and the Human Body: Thermal Spray Science and Applications*, Houston, Texas, USA, May 21-24, 2012, Basil R. Marple, Arvind Agarwal, Laura Filofteia-Toma, Margaret M. Hyland, Yuk-Chiu Lau, Chang-Jiu Li, Rogerio S. Lima, and André McDonald, Ed., ASM International, Materials Park, OH, 2012.

D. Zois, T. Wentz, R. Dey, S. Sampath, and C.M. Weyant, Center for Thermal Spray Research, SUNY, Stony Brook, NY. Contact e-mail: zoisdem@hotmail.com.

which constitute the major components of the process-induced residual stresses (Ref 8).

The HVOF thermal spraying process involves a variety of parameters affecting the in-flight particle properties and their interaction with the substrate, thus the coating build-up itself. These parameters are numbered to be well over 20 (Ref 9), but some of these are reported to be more prominent. Of high importance are mentioned to be: spray distance, (Ref 10, 11), combustion pressure (Ref 12, 13), oxygen-to-fuel ratio (Ref 11), and powder feed rate (Ref 14, 15). Manipulations of these parameters are translated into variations in particle temperature and velocity. Process diagnostic tools enable the measurement of these in-flight properties, thus assisting in the establishment of a first direct link between spraying parameters and coating build-up history and properties. However, there are also additional parameters such as substrate temperature, deposition rate, oxidation, etc., which affect the coating build-up sequence and are not directly controllable, rendering the tailoring of coating properties a very complicated task. An in situ curvature sensor (ICP) (Ref 2) capable of monitoring the deposition and thermal stress as well as the substrate temperature during spraying enables a more critical assessment of this connection. However, an important prerequisite to obtain maximum benefit of these tools is to design a series of spraying experiments that can distinguish each parameter's influence on in-flight particle states initially, and on the coating build-up sequence, secondly.

In the present study, employment of a Taguchi pattern on strategically selected spray runs, determined each one of the four spraying parameters' contribution to coating

properties. Based on the significance of each parameter, a property description model is built. However, this linkage can be comprehensive, only after an initial correlation between the same spraying series and particles' in-flight properties has been established. In that manner, a step by step mechanism of interaction can be constructed allowing a bi-directional correlation between spraying parameters ↔ particle properties ↔ coating stress ↔ coating properties, rendering coating property tailoring feasible.

NiCr was chosen as a model material due to its relevance in numerous HVOF applications including general corrosion resistance, oxidation and corrosion resistance for coal boilers, binder for Cr₃C₂ cermets as well as the principle component of MCrAlY bond coats. The methodology described can generally be extended to other systems with appropriate pre-consideration of powder chemistry, morphology, and size distributions as the interactions will differ depending on these attributes.

2. Experimental

In thermal spraying, stresses mainly arise from three different sources: (i) During spraying: (a) Shrinkage of the spray particles after solidification (quenching stresses), (b) Plastic deformation of an impacted layer and the elastic restitution of the material beneath after the impact (peening stress). From the above, while quenching stresses are tensile in nature, peening stresses are compressive. (ii) During cooling: The subsequent cooling of substrate and coating bonded together from deposition temperature to room temperature determine stresses originating in the contraction mismatch due to the difference in coefficients of thermal expansion (α) between layers, known as thermal stress. These can be either tensile, when $\alpha_c > \alpha_s$, or compressive, when $\alpha_c < \alpha_s$. (iii) A constrained volume change associated with any solid state phase transformation. A more detailed explanation on the nature of stress can be found elsewhere (Ref 1-3). During spraying and after a stable substrate temperature has been achieved, the stress slope ($\Delta\sigma/\Delta t$) is considered to be constant and is called evolving stress. Evolving stress is considered the key component during spraying, since it reflects the particles' pile-up and their cohesion. Provided that each deposited pass is thinner than the substrate, the evolving stress developed by each layer is calculated by the Stoney Formula (Ref 16), whereas thermal stress—post-spraying—is calculated according to Brenner-Senderoff's formula (Ref 2).

An atomized Ni/20%Cr (wt.) powder, with a ($-45 + 5 \mu\text{m}$) nominal size distribution was used for the present study (NI-105, Praxair Surface Technologies Inc.). The powder was sprayed by a hydrogen-fueled Jet-Kote 3000 torch (Deloro Stellite, Inc.) using a 228.6 mm long nozzle. The nozzle inner diameter was 6.35 mm. Spraying was conducted on 1018 AISI steel (228.6 mm × 25.4 mm × 1.6 mm) coupons designed for the in situ curvature measurement sensor (ICP). Particle state was monitored by an Accuraspray sensor (Tecnar, Quebec, Canada). To measure

the particle velocity the principle is based on a time-shift cross-correlation which yields a precise measurement of the time delay from which the velocity can be calculated since the gap between the measuring points is a precisely known constant. In addition, the detectors are filtered at two different colors, allowing the mean particle temperature to be measured using the very well-known twin wavelength pyrometry principle (assumes that the emissivity of the particles is the same for the two wavelengths). Table 1 lists the spraying parameters tabulated in the form of an L9 (3⁴) orthogonal array. Parameter *D* (Combustion pressure) presented some insignificant fluctuation amongst the spraying runs. That is justified by its dual influence from the combined total flow of oxygen and hydrogen mainly and their ratio secondly. Accordingly, minor adjustments had to be made for both gas flows to satisfy simultaneously parameter *C* (Oxygen-Fuel ratio). The three average levels for parameter *D* are: *D*₁—0.31 MPa, *D*₂—0.41 MPa, *D*₃—0.51 MPa. The number of passes was adjusted according to the feed rate in order to produce coatings of similar thickness. The thicknesses of the coatings ranged from 250 to 300 μm .

After the completion of the experimental array, the ANalysis Of VAriance (ANOVA) tool was used to interpret the effect of each factor on each one of the investigated properties. According to ANOVA, the effect of each factor on a property is quantified by means of the variance ratio *F*. A large value of *F* means that the effect of the factor is large compared to the error variance. Also, the larger the value of *F*, the more important this factor is in influencing the process response. After its determination, the *F* ratio is used for the calculation of the contribution percentage of the factor to the property response (Ref 17, 18). The microstructural characterization of the powder and coatings was conducted by SEM-EDX (Leo Zeiss 1550) and optical microscopy (Leica). For the porosity estimation, five fields of view at 200× magnification for each coating were acquired.

As is well known, one of the major roles of HVOF-sprayed NiCr coatings is corrosion protection, by inhibiting the electrolyte from reaching the substrate. The correlation between spraying parameters and corrosion performance can allow the manipulation and/or prediction

Table 1 The experimental conditions in the form of an L9 (3⁴) orthogonal array

Run no.	Feed rate (g/min)	Distance (mm)	Oxygen-Fuel ratio	Combustion pressure (MPa)
c01	20 (1)	152 (1)	1.2 (1)	0.31 (1)
c02	20 (1)	203 (2)	1 (2)	0.41 (2)
c03	20 (1)	254 (3)	0.8 (3)	0.51 (3)
c04	40 (2)	152 (1)	1 (2)	0.51 (3)
c05	40 (2)	203 (2)	0.8 (3)	0.31 (1)
c06	40 (2)	254 (3)	1.2 (1)	0.41 (2)
c07	60 (3)	152 (1)	0.8 (3)	0.41 (2)
c08	60 (3)	203 (2)	1.2 (1)	0.51 (3)
c09	60 (3)	254 (3)	1 (2)	0.31 (1)

The values in brackets indicate the level of each factor

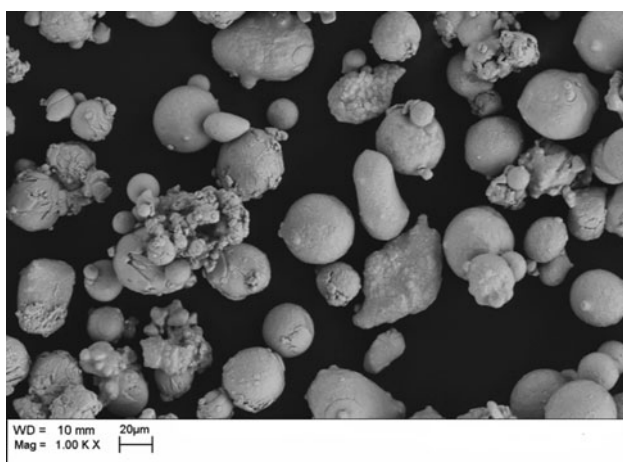
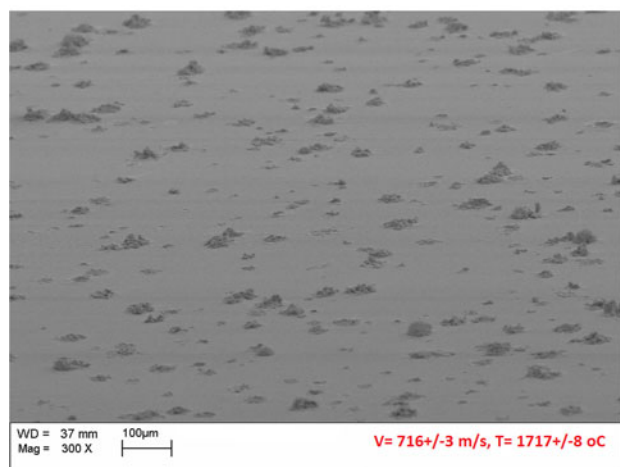
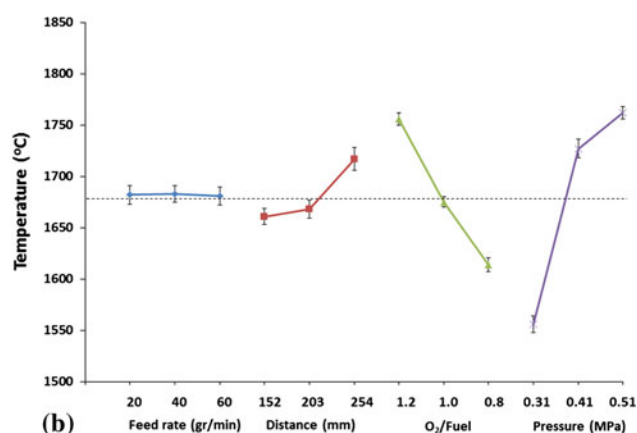
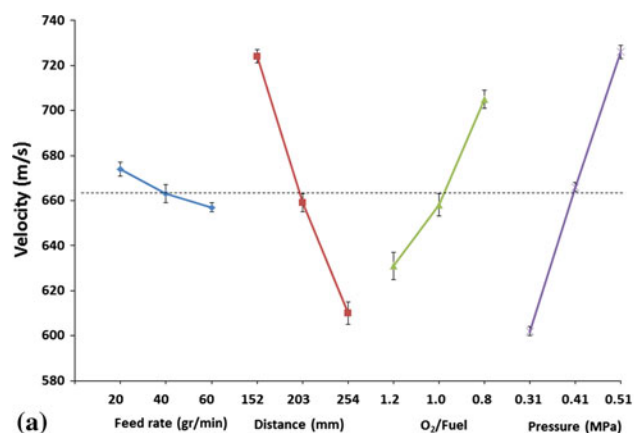
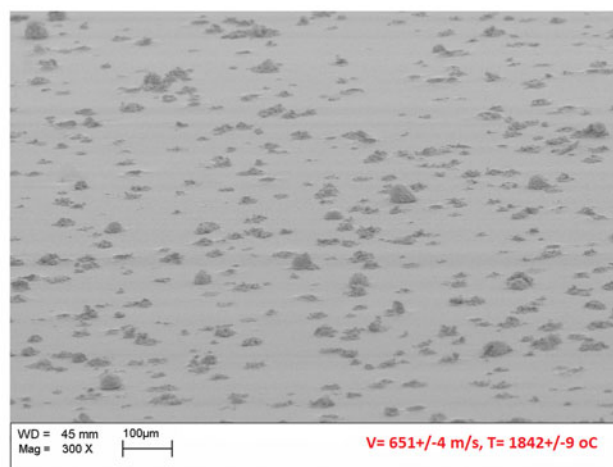


Fig. 1 Ni/20%Cr (wt.) powder particles (BSE detector)



(c)



(d)

Fig. 2 (a) The graphical impact of each parameter on particle velocity, (b) the graphical impact of each parameter on particle surface temperature (the dotted lines indicate the average values), (c) collected particles sprayed with conditions c03F (SE detector), Accuraspray data collected during spraying on the bottom right corner of the picture, (d) collected particles sprayed with conditions c03O (SE detector), Accuraspray data collected during spraying on the bottom right corner of the picture

(1200 grit) coatings' surfaces using a diamond Berkovich indenter. The maximum load applied was 5 N.

3. Results and Discussion

3.1 Particle In-flight Properties

The morphology of the atomized powder is shown in Fig. 1. The graphical effect of each factor in particle in-flight properties is shown in Fig. 2(a) and (b). Table 2 lists the factors' contribution on particle velocity and particle surface temperature. Regarding particle velocity, the most important factors are combustion pressure and distance. Increasing the combustion pressure or decreasing the distance causes the velocity to increase in a roughly linear fashion. Temperature is declining from oxygen-rich (1.2) to fuel-rich ratios (0.8), suggesting oxidation of the particles during their flight. Oxidation occurs due to the high oxidation affinity of Cr. The exothermic reaction of chrome oxides Cr_2O_3 produces enthalpy of -1.14×10^3 KJ/mol (Ref 20) which increases heat on the flying particle. The surface temperature readings of Accuraspray are possibly biased by the oxide formation on the outer shell of the in-flight particles (Ref 8). To prove this assumption, two additional sprayings were conducted. Using an increased raster speed (1000 mm/s) and a low feed rate (3 g/min) one spraying with similar conditions to c03 was conducted (c03F) and one spraying with similar conditions to c03 but with an O_2/F ratio of 1.2 (c03O). The particles were collected on polished steel

Table 2 Contribution percentages for in-flight particle properties and coating evolving stress

	Feed rate (%)	Distance (%)	O_2/F ratio (%)	Combustion pressure (%)
Particle				
Velocity	<1	35.2	14.0	42.2
Temp.	<1	3.7	26.3	64.8
Coating				
Evolving stress	37.3	<1	11.2	50.5
Young's modulus	<1	30.1	2.7	44.9
Microhardness	3.9	36.2	<1	54.6
Porosity	<1	2.4	39.0	29.9
Corrosion				
E_{corr}	<1	35.7	8.2	31.7
E_{p}	<1	25.8	5.1	67.5

plates. Figure 2(c) and (d) shows the particles sprayed under the conditions c03F and c03O, correspondingly. Embedded in the figures are the velocity and surface temperature of the particles measured by Accuraspray. Despite the hotter conditions in the c03O spraying more semi-molten particles, distinguished as lumps, can be seen, thus substantiating the oxide formation bias during the surface temperature readings. The increased particle temperature by an increasing combustion pressure can be justified by prolonged heating during flight, a direct result of the expansion of the flame. In higher combustion pressures the flame is not getting hotter, but it expands in front of the exit of the gun nozzle, extending the supersonic core of the jet (Fig. 3(a), (b), Ref 12). That forces the particles to receive additional heat as they travel through the hot flame core. However, the increased combustion pressure is not completely capable of preventing air entraining into the flame and oxidation still

Table 3 Normalized ratios, the total product of ratios for particle velocity and actual particle velocity

Run no.	Distance	O_2/F ratio	Pressure	Total	Velocity (m/s)
c01	1.00	0.89	0.83	0.74	637 ± 4
c02	0.91	0.93	0.92	0.78	664 ± 3
c03	0.84	1.00	1.00	0.84	721 ± 7
c04	1.00	0.93	1.00	0.93	777 ± 4
c05	0.91	1.00	0.83	0.76	635 ± 4
c06	0.84	0.89	0.92	0.69	577 ± 6
c07	1.00	1.00	0.92	0.92	758 ± 4
c08	0.91	0.89	1.00	0.81	679 ± 7
c09	0.84	0.93	0.83	0.65	534 ± 5

Table 4 Normalized ratios, the total product of ratios for particle surface temperature and actual particle surface temperature

Run no.	Distance	O_2/F ratio	Pressure	Total	Temperature (°C)
c01	0.97	1.00	0.88	0.88	1609 ± 13
c02	0.97	0.95	0.98	0.93	1706 ± 14
c03	1	0.92	1.00	0.92	1719 ± 20
c04	0.97	0.95	1.00	0.95	1738 ± 9
c05	0.97	0.92	0.88	0.81	1475 ± 21
c06	1	1.00	0.98	0.98	1838 ± 13
c07	0.97	0.92	0.98	0.90	1637 ± 7
c08	0.97	1.00	1.00	1.00	1832 ± 15
c09	1	0.95	0.88	0.84	1582 ± 9

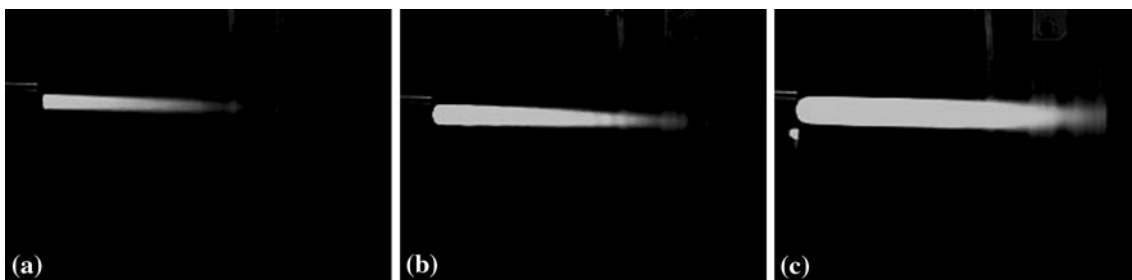


Fig. 3 (a) 0.31 MPa at 1.2 O_2/F ratio, (b) 0.51 MPa at 1.2 O_2/F ratio, (c) 0.31 MPa at 0.8 O_2/F ratio

occurs (Ref 12). At the fuel-rich ratio, the flame is over-expanded, even at low combustion pressure (Fig. 3c), due to unburned fuel ignition during exposure in the air-dissolved oxygen. The additional fuel acts as a shroud which minimizes particle oxidation by consuming any available oxygen molecules. Feed rate plays a negligible role in both particle properties.

3.1.1 Linkage to Process Parameters. A simplified approach was used to allow this linkage. A normalized ratio of each level value to maximum value distinctively for every factor can be obtained, e.g., the distance factor in particle velocity reaches its maximum value in level B_1 : 724 m/s. The three ratios extracted are 1: $B_1/B_1 = 1.00$, 2: $B_2/B_1 = 0.91$, 3: $B_3/B_1 = 0.84$. The same can be repeated for all the factors with non-negligible contribution, in the velocity case again these are also: Pressure and O_2/Fuel

(Fig. 2a). The value of the factor at each spraying parameter combination will be dictated by each level and property measured. Tables 3 and 4, combined with Table 1 as a spraying parameter combination reference are constructed in that manner for particle velocity and temperature, correspondingly. A factor that increases during the progression from level 1 to level 3 (levels shown in brackets in Table 1), can be used as a numerator, whereas a factor that decreases from level 1 to level 3 will be used as a denominator in the total ratio, e.g. distance (D) in Fig. 4a. The products of the normalized ratios of the important parameters, for all spraying runs are shown in Tables 3 and 4, for velocity and surface temperature, correspondingly. In general, the difference between maximum and minimum ratios for a factor is proportional to its contribution to the property response (Table 2).

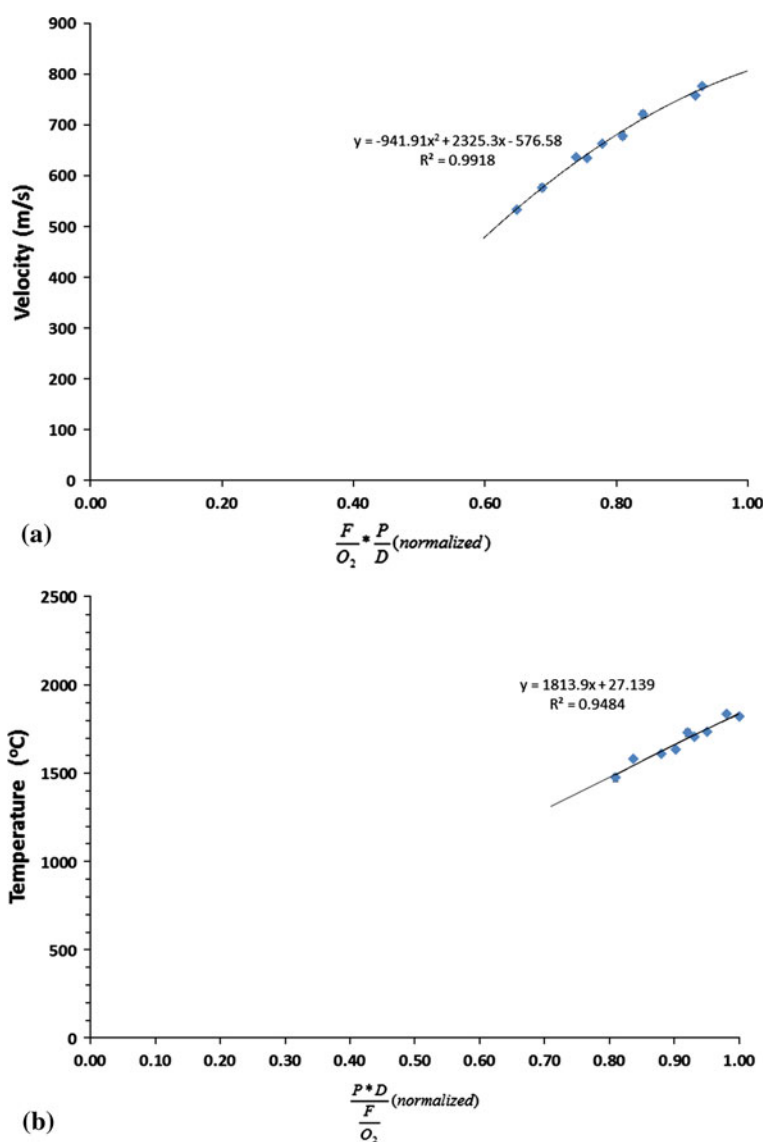


Fig. 4 (a) Plots of velocity as a function of normalized process parameters and (b) surface temperature as a function of normalized process parameters. Note that O_2/F ratio has been inverted as the three chosen levels in Table 1 are in descending order (the dots indicate experimental data, P pressure, D distance)

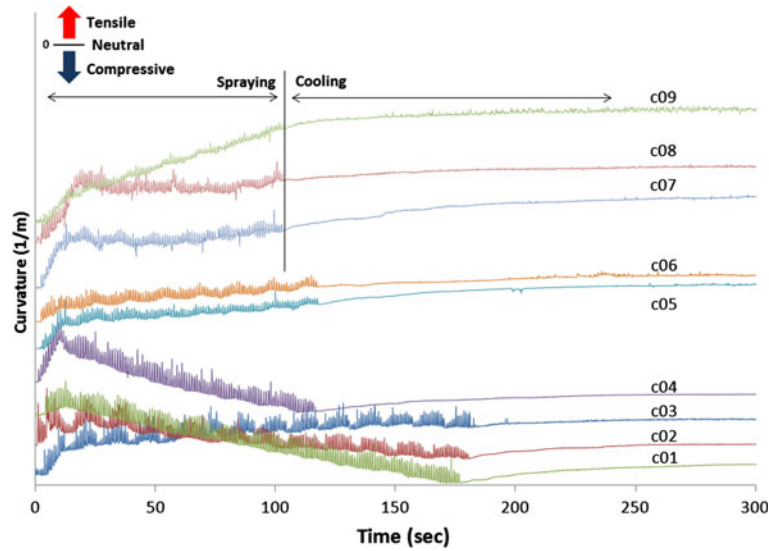


Fig. 5 The spraying and cooling curvatures of each deposited coating as a function of spraying time. The oscillating lines section of each curvature is indicative of the duration of spraying. The spraying and post-spraying cooling stages are shown for runs c07, c08 and c09 (same number of passes)

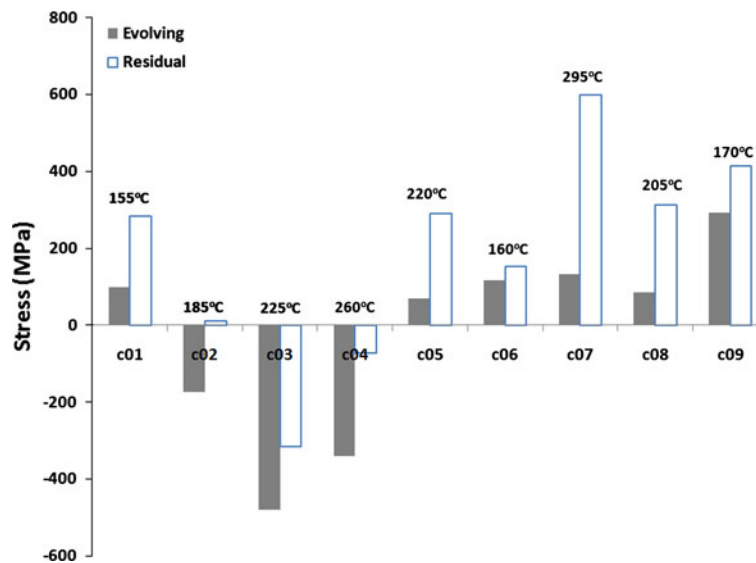


Fig. 6 Evolving and residual stresses distribution in the deposited coatings. The labels indicate substrate temperature during spraying

By plotting the product of total ratios versus actual velocity (Fig. 4a) and actual temperature (Fig. 4b) a generally good approximation can be observed. The approximation enables the description of particle velocity and temperature by process parameter values. Velocity is described more accurately since particle surface temperature is biased by oxidation.

3.2 Coating Deposition

Figure 5 presents the deposition curvatures of the coatings sprayed as a function of time. Different types of evolving stress (compressive, neutral, and tensile) were attained during spraying. All substrates are assumed to

start from a neutral stress status after two pre-heating passes (the pre-heating passes are not included in Fig. 5). The inset drawing in Fig. 5 demonstrates the stress status depending on the direction of the slope. Compressive stresses are noticeable from the descending spraying curvatures, while tensile from the ascending ones. During cooling, an ascending curvature was monitored for all sprayings, indicating tensile stress generation in the coatings. A vertical line demonstrates the end of spraying and the start of post-spraying cooling for coatings c07-c09. The duration of spraying for coatings c01-c03 and c04-c06 was higher since more passes were required to build coatings of similar thickness, due to lower feed rate. The cooling curvature direction was a result of the lower α of the steel

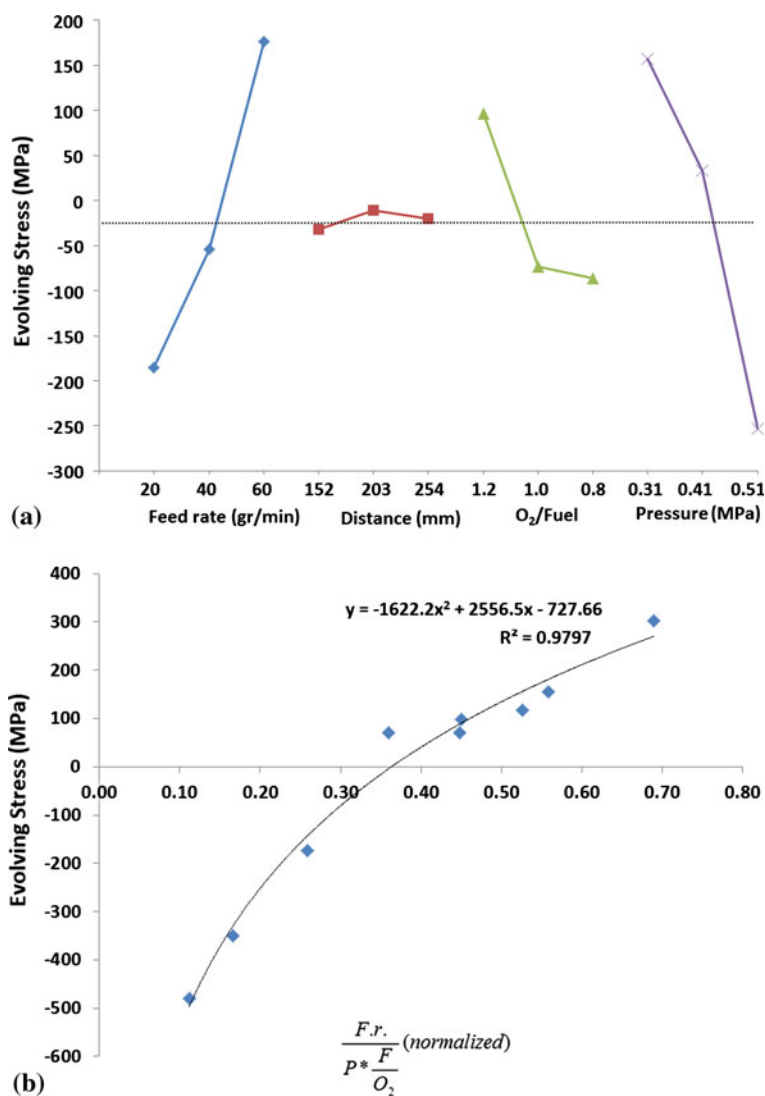


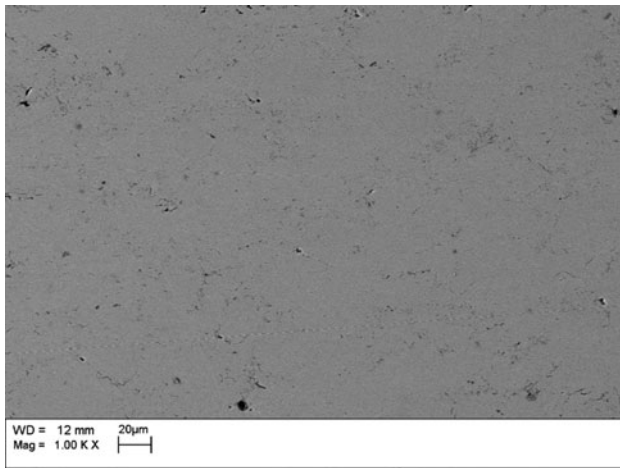
Fig. 7 (a) The graphical impact of each parameter on evolving stress. (b) Evolving stress description as a function of process parameters (the dots indicate experimental data; Fr feed rate)

substrate ($12 \mu\text{m}/(\text{m}^\circ\text{C})$) compared to the coatings' corresponding one ($14.5 \mu\text{m}/(\text{m}^\circ\text{C})$).

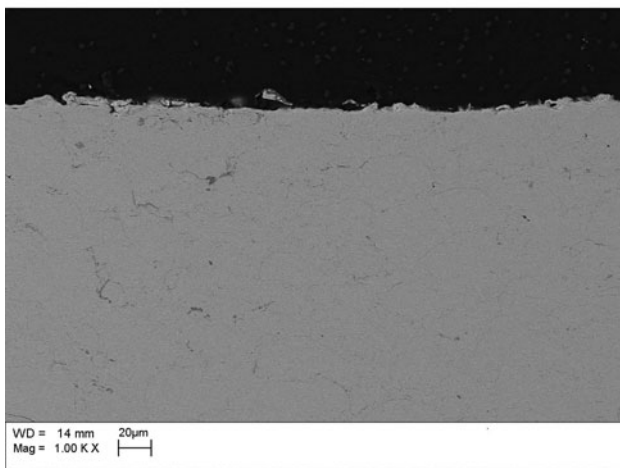
As has been mentioned by previous investigations (Ref 2, 21, 22), post-spraying thermal stresses increase with coating temperature and coating thickness. In the present case, coating thicknesses were kept rather similar, leaving substrate temperature as the main component affecting the curvature ascending degree. It can be noticed in Fig. 6 that generally an increasing substrate temperature expands the gap between evolving and residual stresses, as it amplifies the α_c - α_s difference.

In general, it has been reported that peening intensity is increasing proportionally to particle velocity (Ref 7). However, high particle velocity solely cannot assure compressive evolving stress. As shown in Fig. 7(a) and (b), an increasing feed rate will shift the evolving stress to less compressive and ultimately to a tensile state (60 g/min).

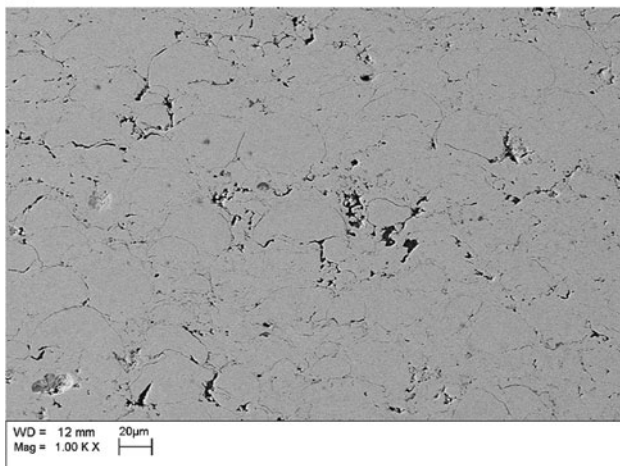
Higher feed rate implies that more particles impinge on pre-deposited splats in every torch pass. As the time intervals between impinging particles are extremely short, they tend to bond in a hot state. Hot surfaces of the solidifying particles promote improved wetting, more rapid heat transfer and therefore increased cohesion. Better intersplat contact is considered to provide a stronger constraint against the contraction of each splat after solidification, which results in a significant increase in the values of quenching stress (Ref 5). Moreover, peening is associated with work hardening of the impacted material. The high temperature of the solidifying particles possibly decreases their work-hardening level as recovery takes place during spraying (Ref 23). It is inferred, hence, that feed rate promotes an increasing quenching stress trend compared to peening stress. By correlating evolving stress with process parameters, according to the procedure



(a)



(b)



(c)

Fig. 8 Cross sections of the deposited coatings (BSE detector). (a) Coating c04, (b) coating c06, (c) coating c09

described above, the plot in Fig. 7(b) can be constructed. According to Fig. 7(b), at the ratio of 0.37, quenching stresses equalize peening stresses. A coating deposited

Table 5 Properties of the deposited coatings

	Young's modulus (GPa)	Hardness (GPa)	Porosity (%)
c01	124 ± 10	2.93 ± 0.49	1.1 ± 0.3
c02	129 ± 21	2.66 ± 0.79	0.8 ± 0.2
c03	142 ± 19	3.41 ± 0.71	1.0 ± 0.3
c04	173 ± 9	5.07 ± 0.53	0.5 ± 0.2
c05	134 ± 8	2.53 ± 0.36	1.2 ± 0.3
c06	122 ± 12	2.63 ± 0.43	1.3 ± 0.3
c07	158 ± 18	3.95 ± 0.41	0.8 ± 0.1
c08	150 ± 11	3.86 ± 0.53	1.1 ± 0.2
c09	115 ± 17	2.40 ± 0.76	1.7 ± 0.4

under the levels of the significant parameters (Feed rate, Combustion Pressure, and Oxygen-Fuel ratio) that satisfy that ratio will present neutral evolving stress. An increase in feed rate or a decrease in combustion pressure shifts the stress to tensile state, while the opposite promotes compressive stress. An oxygen-rich flame seems to promote quenching stress at a limited degree, since it decelerates the particles, as shown in Fig. 2(a). The generally good correlation (Fig. 7b) provides the ability to describe a coating's evolving stress magnitude, by using process parameters. The same correlation for residual stress is more intricate to be employed, since there are additional factors such as the 1st pass curvature, indicative of the adhesion (Ref 7), varying substrate temperature (Fig. 6), etc., that should be considered.

3.3 Coating Properties

Figure 8(a)-(c) exhibit cross sections of coatings c04, c06, and c09, representing compressive, neutral, and tensile evolving stress, respectively, according to Fig. 5. At first glance, denser coatings seem to be associated with more compressive stresses, as will be shown in more detail below. Table 5 lists the deposited coatings' porosity, microhardness, and modulus.

3.3.1 Young's Modulus. The Young's modulus of a coating captures its general health (porosity, interlamellar adhesion, and microcracks) (Ref 2). Additionally, modulus can be related to stress state to some extent: a higher modulus results in greater maintainable quenching stress (Ref 2). Conversely, it has been observed that coatings with higher compressive residual stresses exhibit a higher elastic modulus (Ref 21). Figure 9(a) shows that there is an ambiguous correlation between modulus and evolving stress. After differentiating between different feed rates, an increasing trend of modulus with compressive stress can be discerned. In this manner, similar evolving stress will produce stiffer materials, when they are generated by higher feed rates. The ANOVA tool (Fig. 9b; Table 2) shows that modulus is increased either by adopting shorter spraying distance or by increasing the combustion pressure, suggesting major particle velocity influence. Velocity is the main particle property that affects the coatings' general state since it can place the surfaces of the impinging droplets in a close contact (Ref 24) and thus improve their cohesion (Fig. 9c). The correlation between modulus and process parameters is shown in Fig. 9(d). In

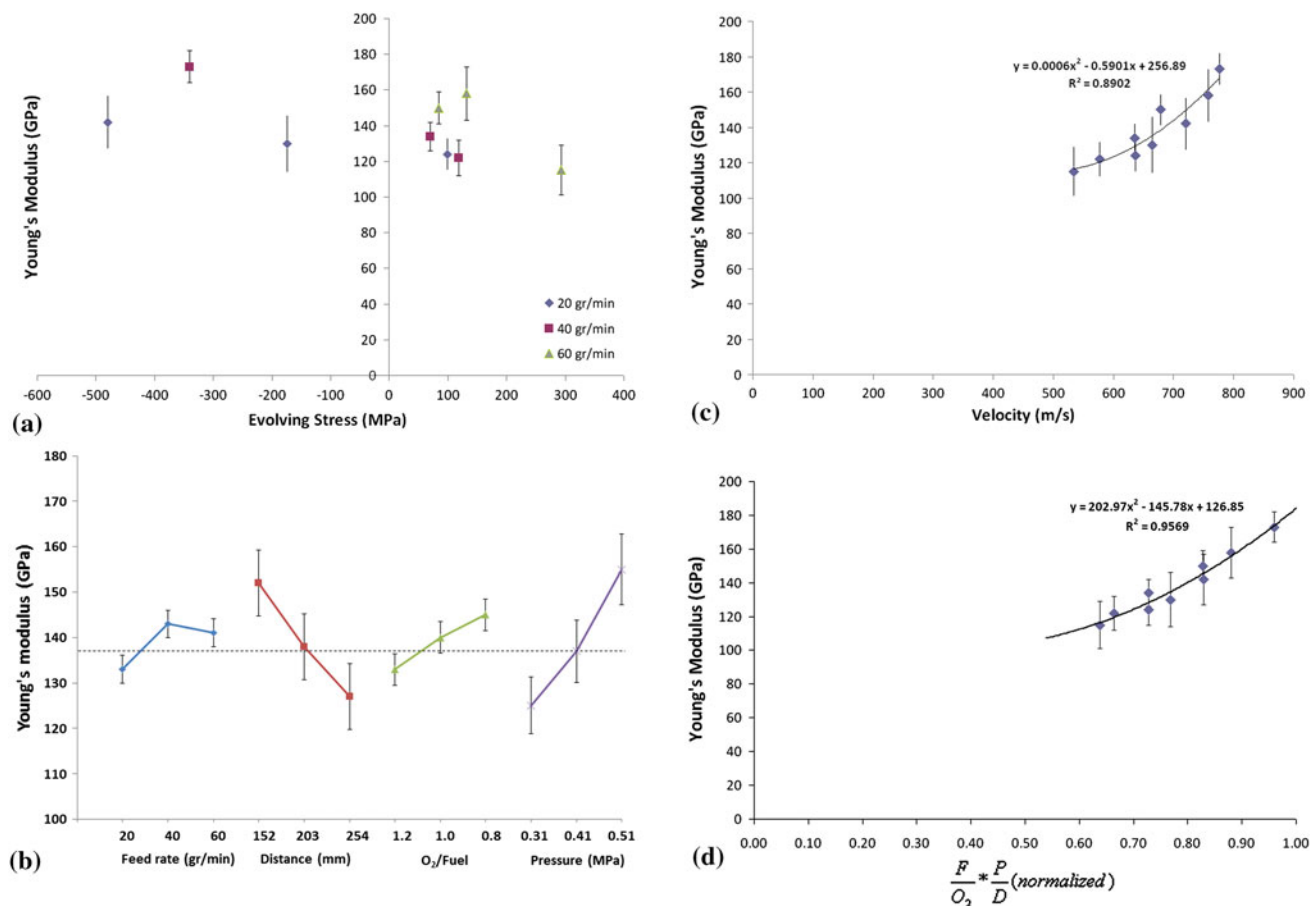


Fig. 9 (a) Young's modulus as a function of evolving stress. (b) The graphical impact of each factor level on Young's modulus (the dotted line indicates the average value). (c) Young's modulus as a function of particle velocity. (d) Coating Young's modulus as a function of process parameters (the dots indicate experimental data)

addition to short distance and high pressure, a fuel-rich flame has a double factor benefit on the coating strength: (i) by increasing particle velocity (Fig. 2a) and (ii) by improving intersplat cohesion, since no peripheral particle oxides are formed.

3.3.2 Microhardness. In HVOF spraying, coating hardness can be increased by work-hardening inflicted on the pre-deposited material due to peening (Ref 25). Work-hardening is intensified as the particle impact velocity increases (Fig. 10a). Figure 10(b) and Table 2 verify that microhardness is increased by the same process parameters that boost velocity. Tuning of the two significant factors (pressure and distance) can yield harder coatings (Fig. 10c), resulting in up to a 110% increase (c04—5.07 GPa, c09—2.40 GPa).

3.3.3 Porosity. Figure 11(a) and Table 2 presents the fluctuation of porosity with process parameters. Higher spraying distance and decreasing combustion pressure seem to raise majorly the porosity levels. Conversely, a fuel-rich flame ensures more efficient melting of the particles, allowing filling of the voids. Porosity seems to be inversely proportional to particle impinging velocity, as they are

affected by the same spraying factors. Figure 11(b) exhibits that generally coatings deposited under compressive stress are associated with denser structures. Uncertainties such as pull-out of sections of particles or even entire particles during polishing and microporosity often found in the splat boundaries (Ref 26) increase the uncertainty of the measurements (Table 5) and consequently decrease the precision of the regression analysis. Figure 11(c) is indicative of the coatings' porosity description as a function of process parameters.

3.4 Corrosion

The potentiodynamic plots of the deposited coatings are exhibited in Fig. 12(a)-(c). For comparison, the potentiodynamic polarization scans of a bulk Ni-20%Cr (wt.) alloy and of the 1018 AISI substrate steel are plotted. The corrosion (E_{corr}) and pitting potentials (E_p), expressing general and local corrosion, are listed in Table 6.

3.4.1 Corrosion potential (E_{corr}). Figure 13(a) illustrates the influence of particle velocity on the corrosion potential (E_{corr}) of the coatings. This correlation can be

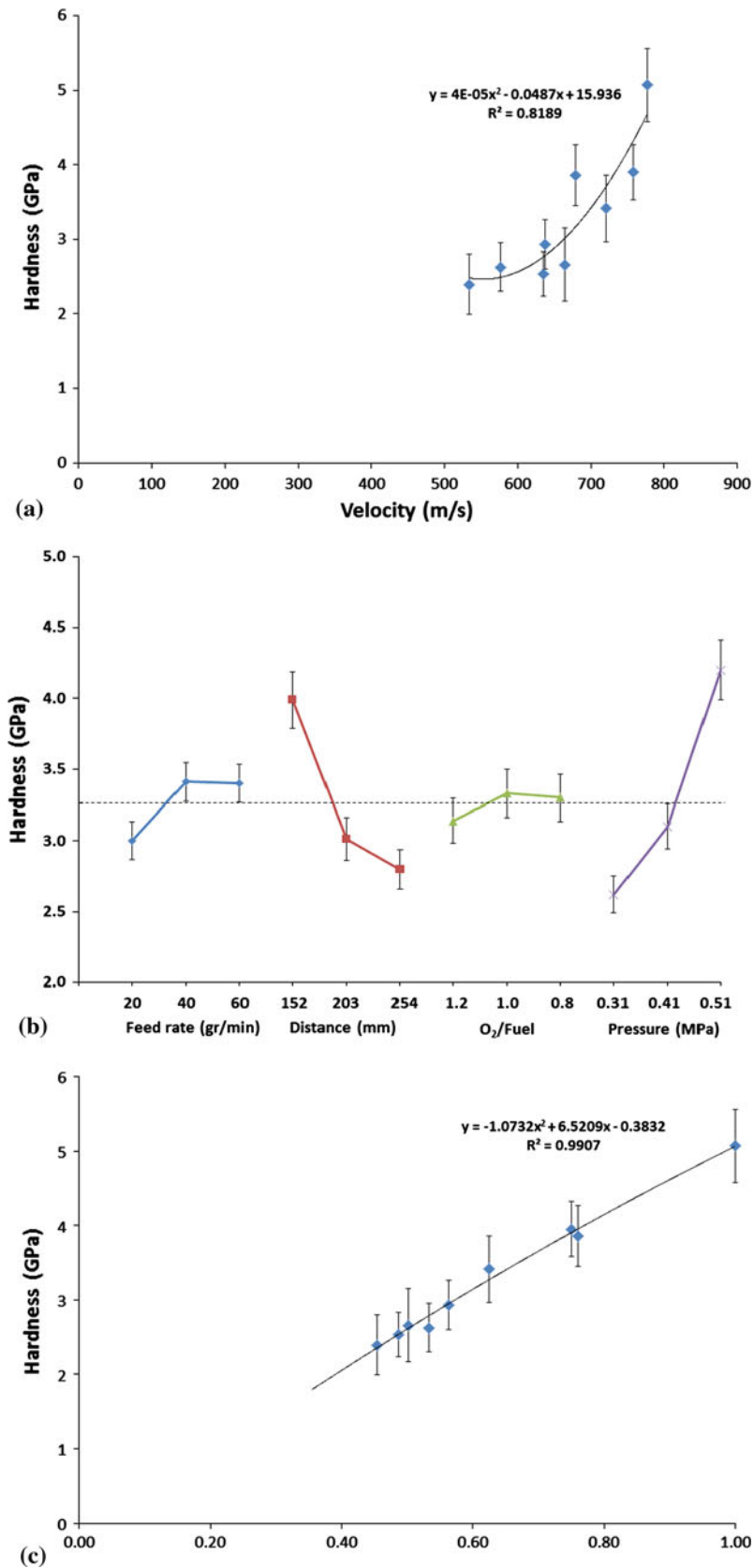


Fig. 10 (a) Microhardness as a function of particle velocity. (b) The graphical impact of each parameter level on microhardness (the dotted line indicates the average value). (c) Microhardness as a function of process parameters (the dots indicate experimental data)

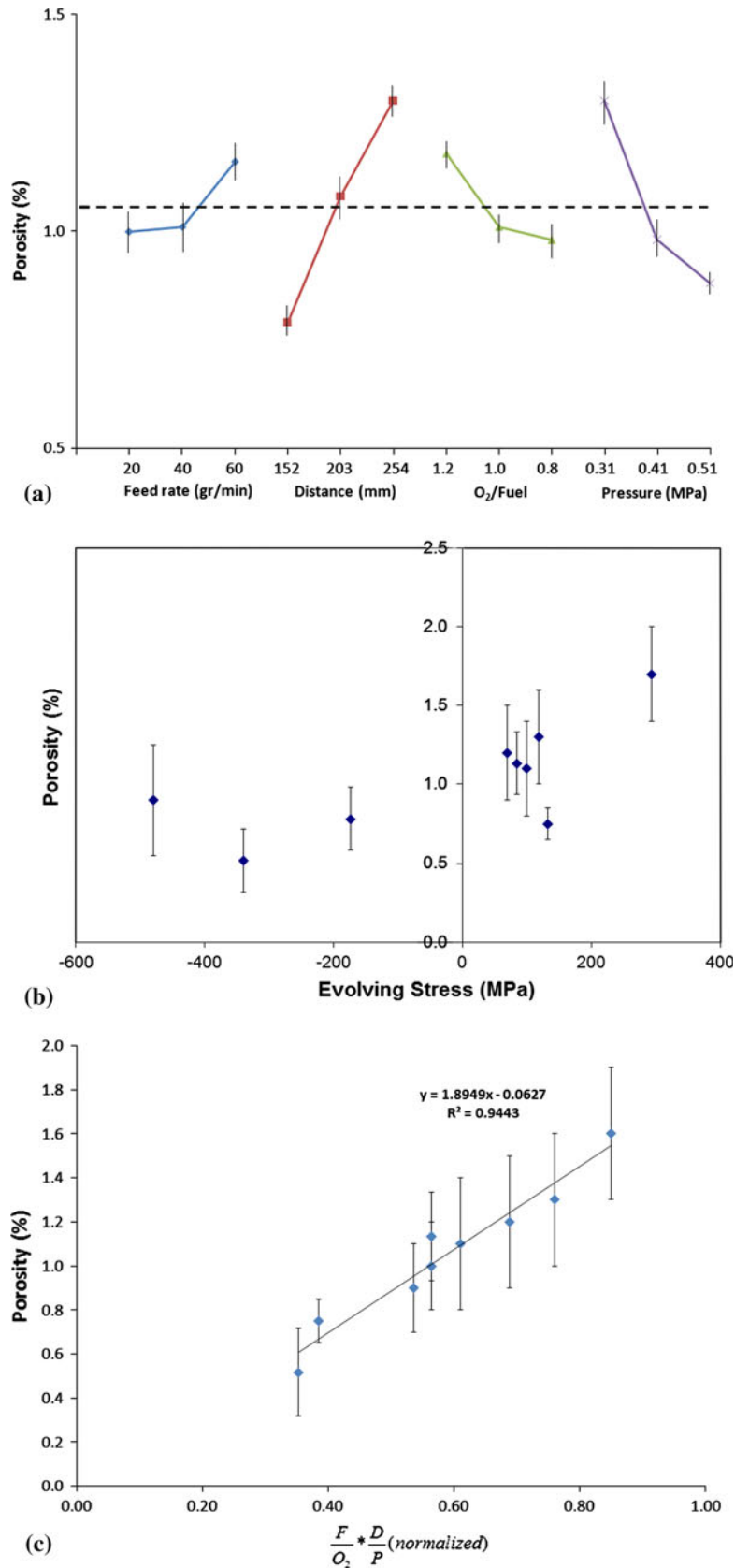


Fig. 11 (a) The graphical impact of each parameter level on porosity (the dotted line indicates the average value), (b) coating porosity as a function of evolving stress, (c) coating porosity as a function of process parameters (the dots indicate experimental data)

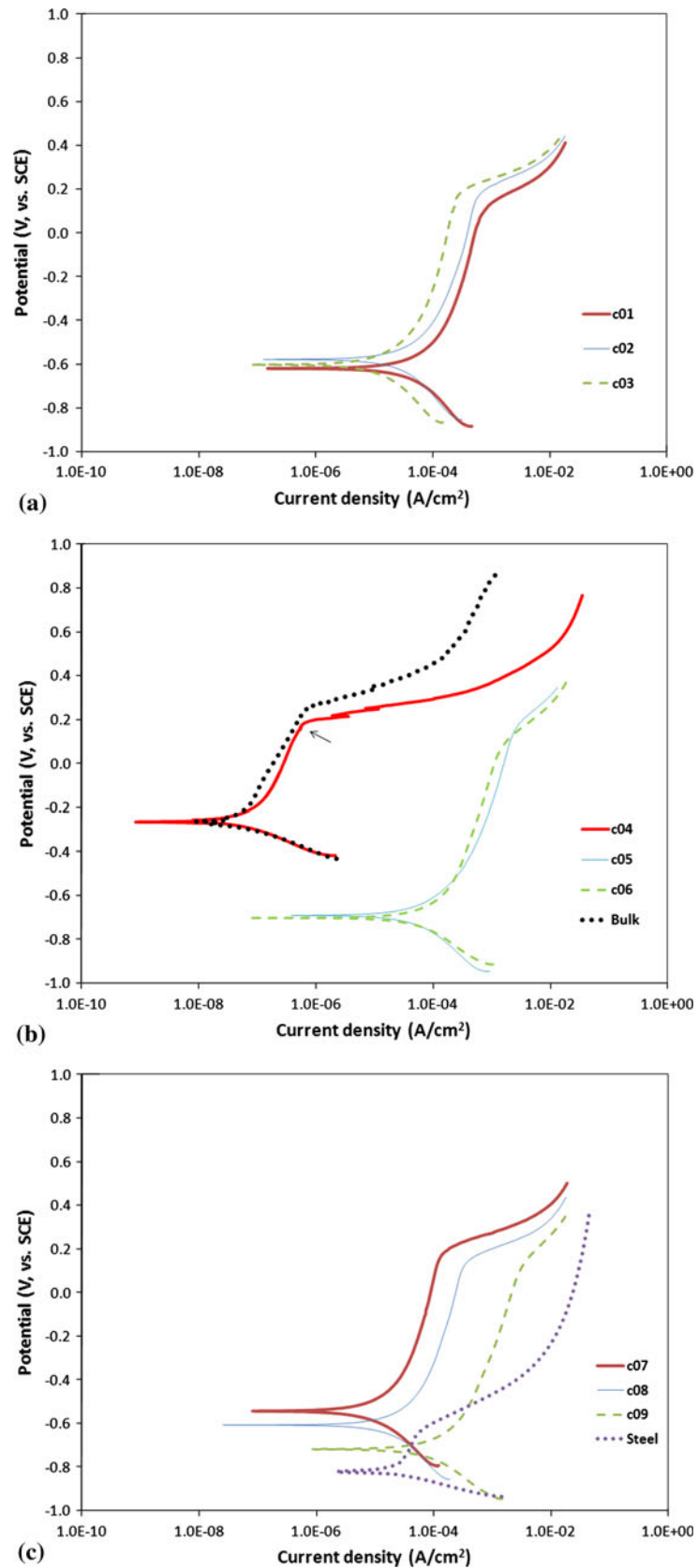


Fig. 12 Potentiodynamic plots of the deposited coatings in 3.5 % (wt.) NaCl. (a) Coatings c01-c03 (sprayed at 20 g/min), (b) coatings c04-c06 (sprayed at 40 g/min) and bulk Ni-20%Cr (wt.), (c) coatings c07-c09 (sprayed at 60 g/min) and 1018 substrate steel

Table 6 Corrosion potentials of the deposited coatings, Ni-20%Cr (wt.) bulk alloy and 1018 AISI substrate steel

	Corrosion potential, E_{corr} (V, vs. SCE)	Pitting potential, E_p (V, vs. SCE)
c01	-0.63 ± 0.07	0.07 ± 0.01
c02	-0.62 ± 0.09	0.14 ± 0.03
c03	-0.60 ± 0.06	0.15 ± 0.03
c04	-0.26 ± 0.05	0.17 ± 0.04
c05	-0.69 ± 0.02	0.13 ± 0.02
c06	-0.70 ± 0.03	0.04 ± 0.02
c07	-0.54 ± 0.07	0.14 ± 0.04
c08	-0.61 ± 0.07	0.08 ± 0.02
c09	-0.72 ± 0.04	0.10 ± 0.03
Bulk Ni-20%Cr (wt.)	-0.26 ± 0.03	0.21 ± 0.04
AISI 1018	-0.83 ± 0.05	-0.42 ± 0.05

justified by an improved intersplat cohesion, reflected by the coatings' modulus as shown above, which minimizes the number of potential passages to the coating-substrate interface (Fig. 13b). Figure 13(c) shows the interrelation between evolving stress and E_{corr} . Generally, under the same feed rate, higher compressive stress results in higher (nobler) coatings' E_{corr} . On the contrary, tensile stresses cannot ensure substrate protection since the particle impact energy is not sufficient to lessen the intrasplat microporosity. From the spraying parameters perspective, spraying distance and combustion pressure influence in a similar manner the particle impact velocity and the corrosion potential, evidencing their correlation, as shown in Fig. 13(d) and Table 2. The normalized product of the significant spraying parameters in Fig. 13(e) allows the E_{corr} to be described and predicted.

3.4.2 Pitting potential (E_p). The pitting potential (E_p) is indicative of the dissolution of the superficial protective thin oxide film which hinders any ions advancement in both directions. The stability of this film is related to the Cr content in the alloy, where higher content designates increased durability in higher potentials, e.g., more aggressive environments (Ref 27). Figure 14(a) shows the correlation between E_p and particle velocity at impact. In the same graph, the repercussion of the flame environment on the coatings' pitting potential is clearly discernible. Coatings deposited by an oxygen-rich flame show lower E_p and thus an inferior performance compared to neutral and fuel enriched flame sprayed coatings. That can be justified by Cr bonding with oxygen molecules to form oxides during spraying, resulting in its depletion in the alloy. For the same reason, decreased particle in-flight time, the pitting potential presents an increasing trend with velocity. The degree of the flame environment influence on the E_p and pressure and distance—both the latter decreasing the flight time—is easily noticeable in the factors effect in Fig. 14(b) and Table 2. Additionally, the oxide formation

in oxygen-rich flame verifies the biased particle surface temperature during spraying, as shown in Fig. 2(b). Figure 14(c) presents the description of E_p as a function of the three significant parameters. Figure 14(d) shows that compressive stresses increase the E_p of coatings when they are sprayed at the same O_2/F ratio.

Coating c04 presented a polarization plot very similar to the one of the bulk Ni-20%Cr (wt.) alloy, as shown in Fig. 12b. This performance can possibly be related to extensive peening, combined with a stoichiometric flame which prevented Cr depletion. Considerable pitting was noticed on the surface of coating c04 (Fig. 15a) for polarization potentials higher than the E_p , which assisted the electrolyte to eventually reach the substrate. Following that, the current density increased rapidly (arrow, Fig. 12b).

As modulus decreases and porosity increases, the electrolyte acquires more passages to the substrate, thus reducing the amount of pitting on the surface of the coatings. When the potential reaches E_p , limited pitting occurs on the surface (coating c07, Fig. 15b), as general corrosion runs laterally. Finally, in coatings of very low modulus and high porosity, such as coating c09, oxides can be traced inside the coating (Fig. 15c-e), suggesting extensive general corrosion of the steel substrate. As the electrolyte penetrates through the coating, paths of increased porosity can be distinguished (Fig. 15c) while in certain cases bulky oxides can be formed too (Fig. 15d-e). The limited current density increase at potentials above E_p , confirms that (Fig. 12c, c09). Concluding, two extreme cases can be defined in the NiCr coatings' corrosion behavior. In coatings demonstrating high modulus and low porosity, such as coating c04, the potentiodynamic plot resembles the plot of the bulk NiCr alloy, where the passive film efficiently protects the material as high as its pitting potential (E_p). On the contrary, coatings of low modulus and high porosity, such as coating c09, present a polarization plot similar to the plot of the steel substrate, suggesting its parallel widespread dissolution. The rest of the coatings presented polarization plots between these two extremes.

Relating the coatings' corrosion performance to spraying parameters, more corrosion-resistant coatings regarding E_{corr} are deposited when sprayed at highest pressure combined with short spraying distance. Fuel-rich or a stoichiometric flame should be used to prevent Cr depletion and to raise the pitting potential.

4. Conclusions

A factorial design of a HVOF spraying series of NiCr powder has been employed to correlate process

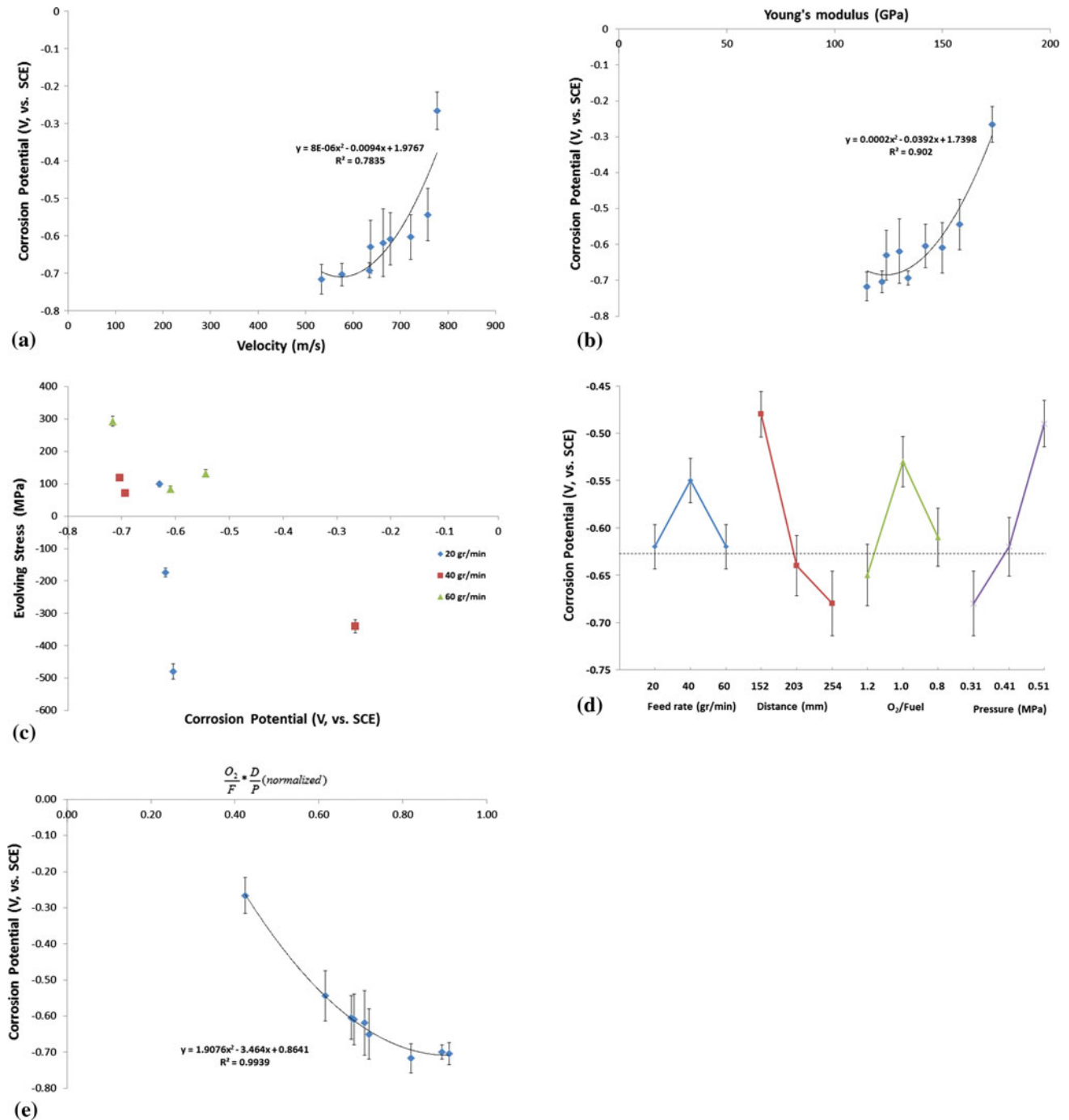


Fig. 13 (a) The coating corrosion potential as a function of particle velocity, (b) the corrosion potential as a function of coating Young's modulus, (c) evolving stress as a function of the corrosion potential, (d) the graphical impact of each parameter level on corrosion potential (the dotted line indicates the average value), (e) the corrosion potential as a function of the process parameters (the dots indicate experimental data)

parameters to in-flight particle properties and coating stress state. Nine coatings of similar thickness were deposited utilizing three distinctive levels of four important spraying parameters. The main conclusions for this study are as follows:

- (1) Concerning particle in-flight properties, combustion pressure and distance were found to have the most profound impact on particle velocity, while O₂/F ratio and combustion pressure influenced particle surface temperature. Particles presented erroneously higher

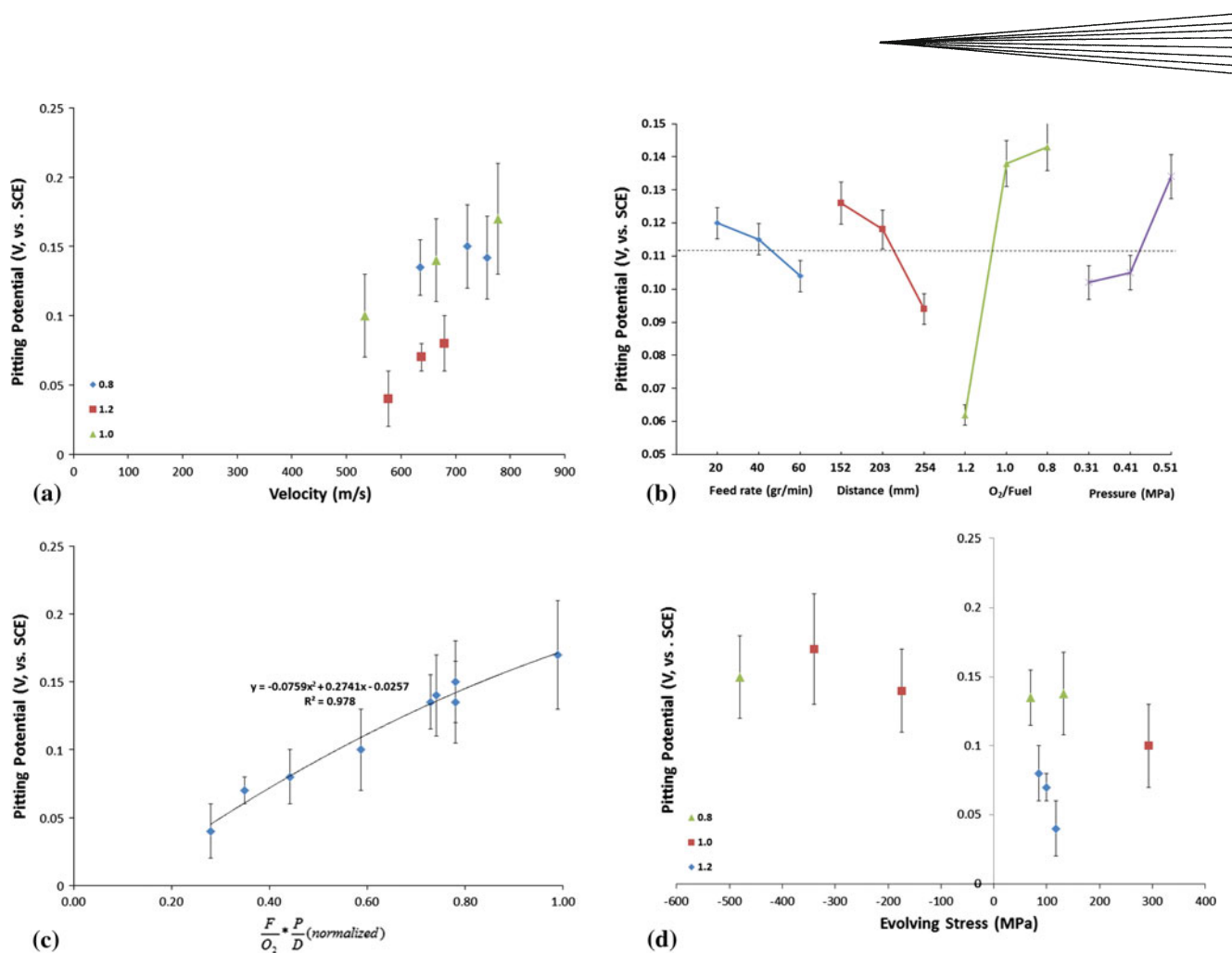


Fig. 14 (a) The pitting potential as a function of particle velocity, (b) the graphical impact of each parameter level on breakaway potential (the dotted line indicates the average value), (c) the breakaway potential as a function of process parameters (the dots indicate experimental data), (d) the breakaway potential as a function of evolving stress

temperature in an oxygen-rich flame as a result of extensive oxidation during spraying.

- (2) By using a product of normalized ratios of each significant factor, in-flight particle properties and coatings' evolving stress and properties can be described by process parameter values. This correlation enables a direct manipulation of the above properties by process parameter adjustments.
- (3) Evolving stresses were affected majorly by two parameters: feed rate and combustion pressure. Combustion pressure acted as leverage for inducing peening stress, as it majorly reflects particle velocity, while feed rate favored quenching stress, due to improved intersplat contact. Above a certain level of powder feed rate, dominant peening in the coating was unachievable. Extensive peening stresses were still present in the coating, but they were overwhelmed by the faster increasing quenching stresses.

- (4) Microhardness and Young's modulus were directly influenced by the particle impinging velocity. From the spraying parameters' perspective, harder and stiffer coatings were deposited under high combustion pressure and short spraying distance. Under the same feed rate, modulus presented an increasing trend with compressive stresses.
- (5) General (E_{corr}) and pitting (E_p) corrosion behavior was improved at a higher particle impinging velocity. Stress-wise, compressive coatings presented an overall better corrosion performance. The flame environment was the major factor influencing the pitting susceptibility of the deposited coatings.

Forthcoming work is planned to add in the correlation portfolio, properties such as coating bond strength, adhesive wear and oxidation resistance, to allow the establishment of a complete mapping of spraying parameters and coating functionality.

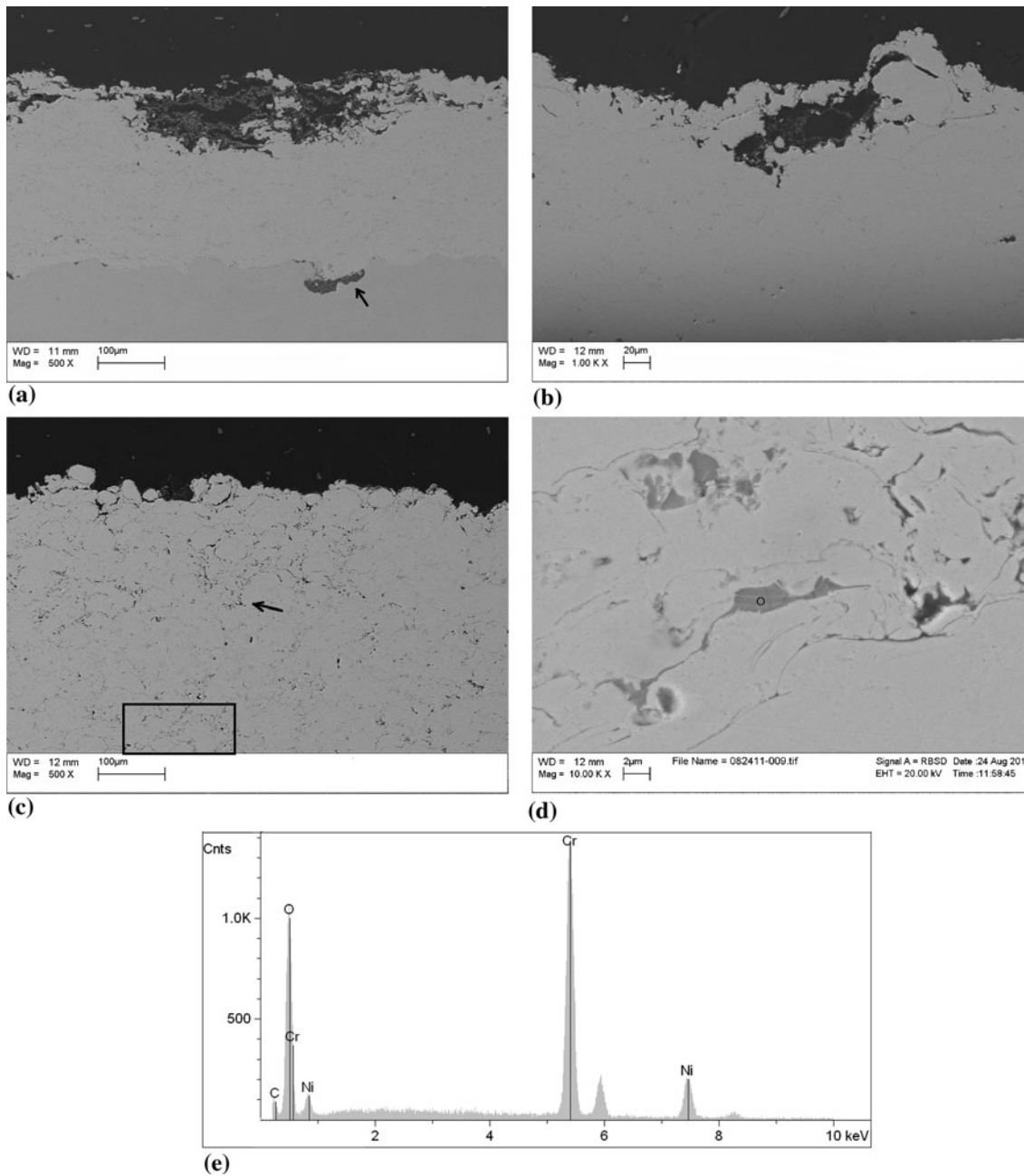


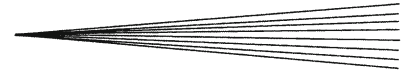
Fig. 15 (a) Pitting corrosion in the surface of coating c04 (cross section, BSE detector). The arrow indicates electrolyte penetration in the substrate underneath the pit. (b) Pitting corrosion in the surface of coating c07 (cross section, BSE detector); (c) oxides path showing electrolyte infiltration in coating c09 as shown by arrow (cross section, BSE detector); (d) higher magnification of the area indicated with rectangle in (c); (e) elemental analysis of the oxide marked in (d)

Acknowledgments

This research was supported in part by the GOALI program of NSF CMMI 1030492 and by the Consortium for Thermal Spray Technology.

References

1. T.W. Clyne and S.C. Gill, Residual Stresses in Thermal Spray Coatings and Their Effect on Interfacial Adhesion: A Review of Recent Work, *J. Therm. Spray Technol.*, 1996, **5**(4), p 401-418
2. J. Matejcek, S. Sampath, D. Gilmore, and R. Neiser, In-situ Measurement of Residual Stresses and Elastic Moduli in Thermal Sprayed Coatings. Part 2: Processing Effects on Properties of Mo Coatings, *Acta Mater.*, 2003, **51**, p 873-885
3. Y.C. Tsui and T.W. Clyne, An Analytical Model for Predicting Residual Stresses in Progressively Deposited Coatings. Part 1: Planar Geometry, *Thin Solid Films*, 1997, **306**, p 23-33
4. S. Sampath, X. Jiang, A. Kulkarni, J. Matejcek, D.L. Gilmore, and R.A. Neiser, Development of Process Maps for Plasma Spray: Case Study for Molybdenum, *Mater. Sci. Eng. A*, 2003, **348**, p 54-66



5. S. Kuroda, T. Dendo, and S. Kitahara, Quenching Stress in Plasma Sprayed Coatings and Its Correlation with the Deposit Microstructure, *J. Therm. Spray Technol.*, 1995, **4**(1), p 75-84
6. E. Dongmo, M. Wenzelburger, and R. Gadow, Analysis and Optimization of the HVOF Process by Combined Experimental and Numerical Approaches, *Surf. Coat. Technol.*, 2008, **202**, p 4470-4478
7. S. Kuroda, Y. Tashiro, H. Yumoto, S. Taira, H. Fukanuma, and S. Tobe, Peening Action and Residual Stresses in High-Velocity Oxygen Fuel Thermal Spraying of 316L Stainless Steel, *J. Therm. Spray Technol.*, 2001, **10**(2), p 367-374
8. A. Valarezo, W.B. Choi, W. Chi, A. Gouldstone, and S. Sampath, Process Control and Characterization of NiCr Coatings by HVOF-DJ2700 System: A Process Map Approach, *J. Therm. Spray Technol.*, 2010, **19**(5), p 852-865
9. L. Pawlowski, *The Science and Engineering of Thermal Spray Coatings*, Wiley, Chichester, 1995
10. B. Rajasekaran, G. Mauer, R. Vaßen, A. Röttger, S. Weber, and W. Theisen, Thick Tool Steel Coatings Using HVOF Spraying for Wear Resistance Applications, *Surf. Coat. Technol.*, 2010, **205**, p 2449-2454
11. J. Saaedi, T.W. Coyle, H. Arabi, S. Mirdamadi, and J. Mostaghimi, Effects of HVOF Process Parameters on the Properties of Ni-Cr Coatings, *J. Therm. Spray Technol.*, 2010, **19**(3), p 521-530
12. C.M. Hackett, G.S. Settles, and J.D. Miller, On the Gas Dynamics of HVOF Thermal Sprays, *Proceedings of the 1993 National Thermal Spray Conference*, C.C. Berndt and T.F. Bernecki, Ed., 7-11 June 1993, Anaheim, CA, p 167-172
13. Y. Ishikawa, J. Kawakita, S. Osawa, T. Itsukaichi, Y. Sakamoto, M. Takaya, and S. Kuroda, Evaluation of Corrosion and Wear Resistance of Hard Cermet Coatings Sprayed by Using an Improved HVOF Process, *J. Therm. Spray Technol.*, 2005, **14**(3), p 384-390
14. X.C. Zhang, B.S. Xu, Y.X. Wu, F.Z. Xuan, and S.T. Tu, Porosity, Mechanical Properties, Residual Stresses of Supersonic Plasma-sprayed Ni-based Alloy Coatings Prepared at Different Powder Feed Rates, *Appl. Surf. Sci.*, 2008, **254**(13), p 3879-3889
15. E. Lugscheider, C. Herbst, and L. Zhao, Parameter Studies on High-Velocity Oxy-Fuel Spraying of MCrAlY Coatings, *Surf. Coat. Technol.*, 1998, **108-109**, p 16-23
16. G.G. Stoney, The Tension of Metallic Films Deposited by Electrolysis, *Proc. R. Soc. Lond. A*, 1909, **82**, p 172-175
17. M.S. Phadke, *Quality Engineering Using Robust Design*, Englewood Cliffs, PTR Prentice Hall, 1989
18. D. Zois, A. Lekatou, M. Vardavoulias, T. Vaimakis, and A.E. Karantzalis, Partially Amorphous Stainless Steel Coatings: Microstructure, Annealing Behaviour and Statistical Optimization of Spray Parameters, *Surf. Coat. Technol.*, 2011, **206**, p 1469-1483
19. W.C. Oliver and G.M. Pharr, Measurement of Hardness and Elastic Modulus by Instrumented Indentation: Advances in Understanding and Refinements to Methodology, *J. Mater. Res.*, 2004, **19**(1), p 3-20
20. A.D. Mah, Heats of Formation of Chromium Oxide and Cadmium Oxide from Combustion Calorimetry, *J. Am. Chem. Soc.*, 1954, **76**(13), p 3363-3365
21. A. Vaidya, T. Streibl, L. Li, S. Sampath, O. Kovarik, and R. Greenlaw, An Integrated Study of Thermal Spray Process-Structure-Property Correlations: A Case Study for Plasma Sprayed Molybdenum Coatings, *Mater. Sci. Eng. A*, 2005, **403**, p 191-204
22. R. Ghafouri-Azar, J. Mostaghimi, and S. Chandra, Modeling Development of Residual Stresses in Thermal Spray Coatings, *Comp. Mater. Sci.*, 2006, **35**, p 13-26
23. A. Itoh, M. Hirata, and M. Ayagaki, Effects of Substrate Temperature During Spraying on the Properties of Sprayed Coatings, *Proceedings of the 1993 National Thermal Spray Conference*, C.C. Berndt and T.F. Bernecki, Ed., 7-11 June 1993, Anaheim, CA, p 593-600
24. V.V. Sobolev and J.M. Guilemany, Effect of Substrate Deformation on Droplet Flattening in Thermal Spraying, *Mater. Lett.*, 1998, **35**, p 324-328
25. S. Kuroda, Properties and Characterization of Thermal Sprayed Coatings-A Review of Recent Research Progress, Thermal Spray, Meeting the Challenges of the 21st Century, *Proceedings of the 15th International Thermal Spray Conference*, C. Coddett, Ed., 25-29 May 1998, France, ASM International, p 539-550
26. R. McPherson, A Review of Microstructure and Properties of Plasma Sprayed Ceramic Coatings, *Surf. Coat. Technol.*, 1981, **39**(40), p 173-181
27. E.E. Stansbury and R.A. Buchanan, *Fundamentals of Electrochemical Corrosion*, ASM international, Materials Park, 2000